

Cylindrical Direct-Current Triboelectric Nanogenerator with Constant Output Current

Jianlong Wang, Yikang Li, Zhijie Xie, Yuhong Xu, Jianwen Zhou, Tinghai Cheng,*
Hongwei Zhao,* and Zhong Lin Wang*

In this article, a cylindrical direct-current triboelectric nanogenerator (DC-TENG) that can generate an almost constant current output with a low crest factor by phase coupling is reported for the first time. Here, the influence of phases (P) and groups (G) on the DC-TENG is investigated. Experiments show that the crest factor of current, significantly decreases as the phases increase, and the output performance significantly increases as the groups increase. One phase triboelectric power-generating unit of the DC-TENG with three-phase and five-group (3P5G) produces an open-circuit voltage of 149.5 V, short-circuit current 7.3 μ A, and transferred charge of 56.7 nC at 600 rpm. The DC-TENG can produce a coupling current of 21.6 μ A and the average output power of 2.04 mW after each phase output is rectified and superimposed. Additionally, the crest factor of output current is reduced to 1.08, and the high-performance characteristics of an almost constant direct-current is achieved. The research is of considerable significance to the practical applications of TENGs in powering sensors of low consumption.

1. Introduction

With the continuous growth of the economy in recent years, the demand for energy is increasing rapidly, and there is even a certain degree of energy crisis.^[1] Thus, many countries around the world have been actively investing in the development and utilization of new green energy.^[2]

Various forms of generators, including electromagnetic generator, piezoelectric generator, triboelectric nanogenerator, etc, play irreplaceable roles in harvesting energy. Triboelectric nanogenerators (TENGs), which is based on the coupling of electrification effect and electrostatic induction effect, are first proposed by Wang group.^[3] The working modes of TENGs could be classified into four types: vertical contact-separation mode, contact-sliding mode, single-electrode mode, and freestanding triboelectric-layer mode.^[4]

TENGs, which have incomparable superiority to harvest various forms of mechanical energy in the low-frequency environment,^[5] are likely to make a significant contribution to the sustainable development of energy in the whole world.^[6]

As is known to all, the most of electronic devices operated using direct current. So far, the methods of converting mechanical energy into direct current are mainly divided into the following types. First, electric brushes are adopted to convert alternating current into direct current without a rectifier bridge, which is uncomplicated in structure.^[7] Second, the working principle of the electrostatic breakdown is that charges transfer from one electrode to the other via an external circuit, then flow back through the ionized air channel generated by electrostatic breakdown.^[8] Third, in the field of materials and chemical industry, Schottky diodes show an uncommon conversion ability to generate direct current without rectification.^[9] Finally, for the way of phase coupling, multiphase TENG could generate a constant direct current with a low crest factor.^[10] Besides, some other novel methods of converting alternating-current into direct-current that contributed to the practical application of TENGs.^[11] Nevertheless, a significant limitation of TENGs is that there exist instantaneous pulses, whose result is that TENGs have a high crest factor.^[10b] Such TENGs with a high crest factor will only bring additional losses and other

J. Wang, Y. Xu, J. Zhou, Prof. T. Cheng, Prof. Z. L. Wang
Beijing Institute of Nanoenergy and Nanosystems
Chinese Academy of Sciences
Beijing 100083, China
E-mail: chengtinghai@binn.cas.cn; zhong.wang@mse.gatech.edu

J. Wang, Y. Li, Y. Xu, J. Zhou, Prof. T. Cheng
School of Mechatronic Engineering
Changchun University of Technology
Changchun, Jilin 130012, China

Z. Xie
School of Mechatronics Engineering
Harbin Institute of Technology
Harbin, Heilongjiang 150001, China

Prof. H. Zhao
School of Mechanical and Aerospace Engineering
Jilin University
Changchun, Jilin 130022, China
E-mail: hwzhao@jlu.edu.cn

Prof. Z. L. Wang
School of Materials Science and Engineering
Georgia Institute of Technology
Atlanta, GA 30332-0245, USA

 The ORCID identification number(s) for the author(s) of this article can be found under <https://doi.org/10.1002/aenm.201904227>.

DOI: 10.1002/aenm.201904227

adverse effects for the electronic devices but also influence the efficiency of energy storage.

To address the issues of high crest factor, a high-performance cylindrical direct-current triboelectric nanogenerator (DC-TENG) is proposed. The DC-TENG utilizes freestanding triboelectric-layer mode, which can generate a high and continuous output with a higher frequency. It mainly consists of a rotator and a cylindrical stator. And the flexible fluorinated ethylene propylene (FEP) films on the rotator are in contact with each phase triboelectric power-generating unit regularly shifted on the cylindrical stator. The structure of blades whose distinguishing feature is flexible contact is adopted in the DC-TENG to reduce the abrasion in the process of mutual sliding. The DC-TENG with three-phase and five-group (3P5G) could generate an almost constant current with a crest factor of 1.08,

and the charging efficiency has increased almost three times. In consideration of the practical application, the wind environment is simulated and a commercial thermometer is operated steadily by the DC-TENG with 3P5G. The DC-TENG has provided potential applications in converting mechanical energy into electrical energy to power the electronic devices of low consumption.

2. Results and Discussion

2.1. Structure Design and Working Principle

The prototype schematic of the direct-current triboelectric nanogenerator (DC-TENG) is demonstrated in **Figure 1**. It mainly

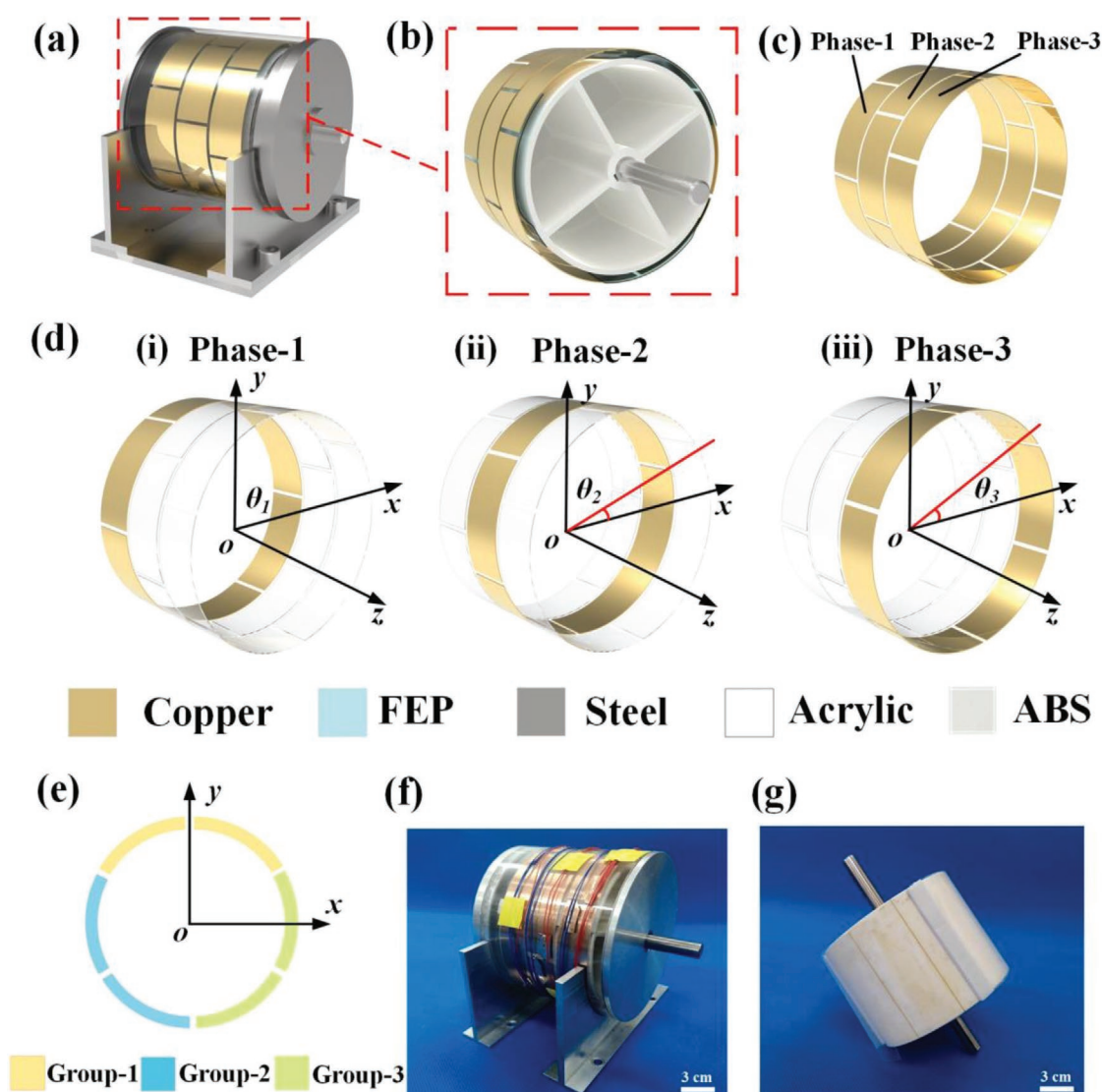


Figure 1. Prototype schematic of the direct-current triboelectric nanogenerator (DC-TENG). a) Schematic diagram showing the monolithic construction of the DC-TENG. b) Partial enlargement drawing of the triboelectric power-generating unit. c, d) Schematic diagram of the structural relationship between each phase triboelectric power-generating unit (the number of phases $P = 3$). e) Schematic diagram of one phase triboelectric power-generating unit (the number of groups $G = 3$). f, g) Photograph of the fabricated DC-TENG and the rotator (scale bar, 3 cm).

contains a rotator and a cylindrical stator (see Figure 1a,b). The rotator consists of a shaft, a reel, and triboelectric materials (i.e., blades made by fluorinated ethylene propylene (FEP) film). In particular, the reel is connected with triboelectric materials by sponge rubbers (illustrated in Figure S1, Supporting Information). The cylindrical stator is composed of an acrylic barrel, two end-caps, two supports, and triboelectric power-generating units. Two end-caps integrated with two bearings are fixed on the acrylic barrel on both sides as the stabilization of shaft. And the acrylic barrel is placed in two supports, and triboelectric power-generating units that are made by copper foils are stuck into the inner wall of the acrylic barrel. To describe the structure of triboelectric power-generating units, the DC-TENG with three-phase and three-group (3P3G) is taken as an example over here. The meaning of three-phase (3P) is that the DC-TENG is in possession of three phases of triboelectric power-generating units (depicted in Figure 1c), and the meaning of three-group (3G) is that each phase triboelectric power-generating unit contains three groups of electrodes in parallel (as is depicted in Figure 1e, the electrodes are divided into three colors to distinguish the different groups). Figure 1f,g shows the photograph of fabricated DC-TENG and rotator. For the DC-TENGs with single-phase and three-group (1P3G), two-phase and three-group (2P3G), and three-phase and three-group (3P3G), the number of blades is 3. For the DC-TENGs with three-phase and four-group (3P4G) and three-phase and five-group (3P5G), the number of blades is 4 and 5, respectively. The number of blades is equal to the number of electrodes groups of each phase triboelectric power-generating unit.

The relationship between each phase triboelectric power-generating units is depicted in Figure 1d. Additional concrete information about remaining DC-TENGs is depicted in Figure S2 (Supporting Information). The first phase triboelectric power-generating unit of the DC-TENG is taken as the reference, and the angle of θ_1 is set as 0° . The angle of θ_2 between the first phase triboelectric power-generating unit and the second one of DC-TENGs can be summarized as

$$\theta_2 = \frac{360^\circ}{N \times P \times G} \quad (1)$$

where N is the number of electrodes per group ($N = 2$), P is the number of phases ($P = 1, 2, 3$), and G is the number of groups per electrode ($G = 3, 4, 5$).

The angle relationship between θ_2 and θ_3 can be determined by

$$\theta_3 = 2\theta_2 \quad (2)$$

where θ_3 is the angle between the first phase triboelectric power-generating unit and the third one of DC-TENGs. Some concrete information is illustrated in Table 1.

The working principle of the DC-TENG is illustrated in Figure 2. Blades whose materials are FEP films are mounted onto the rotator using an adhesion layer. The triboelectric power-generating unit adheres to the inner wall of the acrylic barrel (see Figure S3, Supporting Information). Therefore, blades sweep each triboelectric power-generating unit regularly shifted at the same time. The working principle of DC-TENG

Table 1. The angular relationship between each triboelectric power-generating unit.

	θ_1	θ_2	θ_3
1P3G	0°	N/A ^{a)}	N/A ^{a)}
2P3G	0°	30°	N/A ^{a)}
3P3G	0°	20°	40°
3P4G	0°	15°	30°
3P5G	0°	12°	24°

^{a)}DC-TENGs with 1P3G and 2P3G have only one phase triboelectric power-generating unit and two phases triboelectric power-generating unit, respectively, so the data are not available.

at three states could be emerged in Figure 2a. At the state-1, it can be seen that blades are in contact with electrode-1 of phase-1. In virtue of the electrification effect, the electrons in the electrode-1 transfer to the surface of the FEP films resulting from the electronegativity of the FEP materials and the electropositivity of the copper. At the moment, the FEP films and the electrode-1 are in the condition of electrostatic equilibrium. At the moment, the contact area between blades and the electrode-2 increases for phase-2. To maintain electrostatic balance, the electrons in the electrode-1 transfer to the electrode-2 via the external circuit. The results are that the positive charge of electrode-1 gradually accumulates, and the current of electrode-2 flows into electrode-1 via an external circuit. For phase-3, the FEP films begin to contact with the electrode-1, the electrons in electrode-1 are transferred into electrode-2 via an external circuit, whose result is that reverse alternating. And then, with the rotation of the rotator, the FEP films are in the state-2 and state-3, respectively. The superposition of each phase rectified current generates an almost constant current with a low crest factor. Figure 2b shows the output current generated by each triboelectric power-generating unit regularly shifted. The amplitude of each phase current is basically the same, but there exist regularly shifted phases. Furthermore, a 3D simulation results by COMSOL is employed to clarify the working principle in terms of the DC-TENG to demonstrate the viability of the prototype (see Figure 2c). The materials used in COMSOL are FEP (blades) and Cu textile (electrode), and they were designed to have a similar size as the structure of the actual DC-TENG. What is more, the charge density on the surface of FEP film is assumed as $0.000006 \text{ C m}^{-2}$, and the surface of the electrode is set as a corresponding positive charge, respectively. Finally, the potential distribution diagram is designed. Additional concrete information of 3D simulation results by COMSOL about remaining DC-TENGs is depicted in the Supporting Information (see Figure S4, Supporting Information).

2.2. Output Performance

For the DC-TENG, it is the important factor that each phase triboelectric power-generating unit has a continuous and identical electric output. There are different relationships of phases between each phase triboelectric power-generating units. To

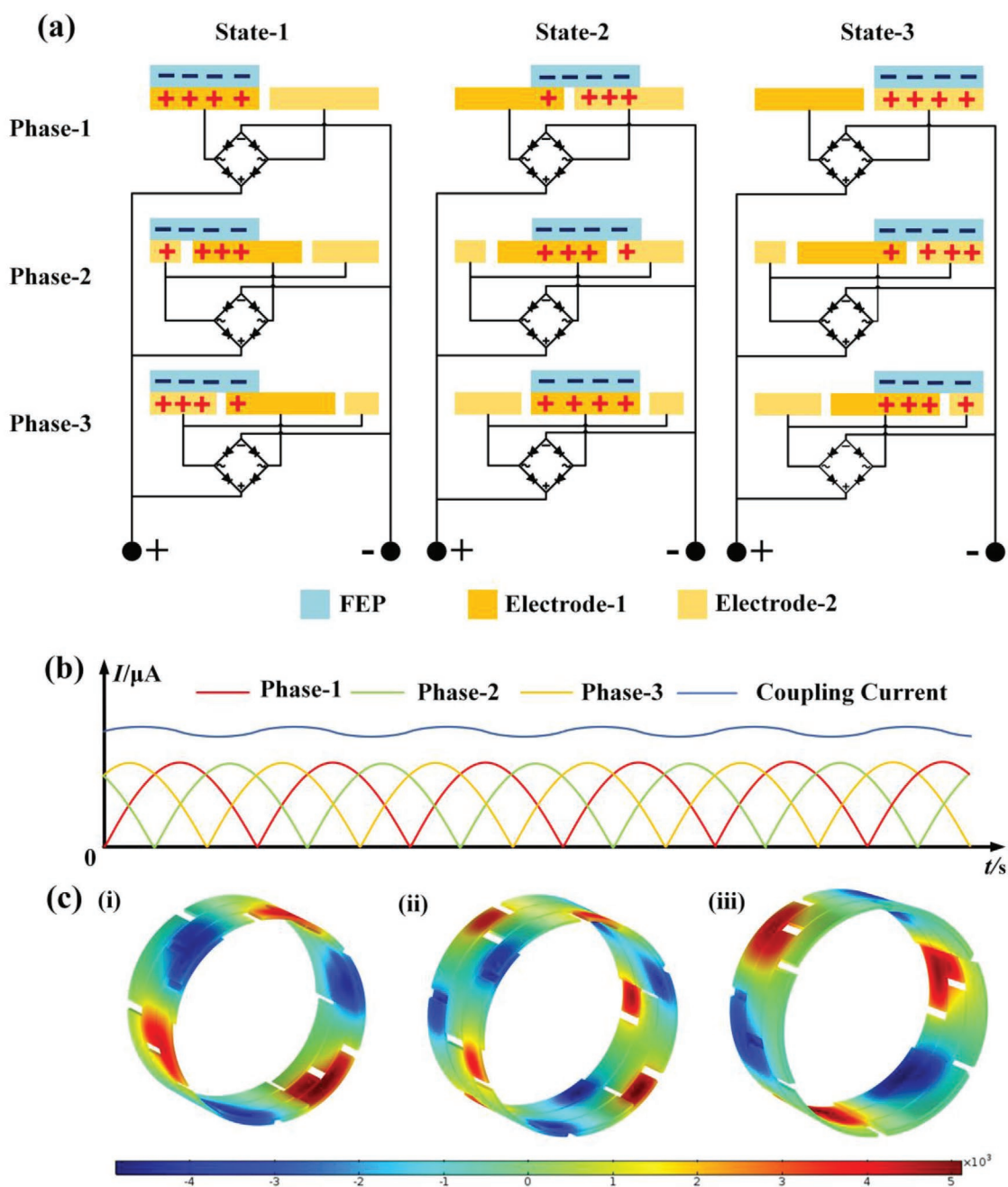


Figure 2. Schematic diagram of the working principle of the DC-TENG. a) Schematic working principle of DC-TENG at three states. b) Schematic diagram of each phase current at a different time. c) 3D simulation results by COMSOL are employed to clarify the working principle of the DC-TENG at three positions.

measure the total output performance of the DC-TENG, a method is adopted that the alternating current output rectified by a full-wave rectifier bridge is superimposed. Each phase triboelectric power-generating units of the DC-TENG having regularly shifted phase is under the condition of guaranteeing the same output performance, and the rectified alternating current is superimposed, generating an almost constant direct-current output.

Furthermore, the output performance of DC-TENGs is influenced by the length of blade and triboelectric materials.

Compared with the polytetrafluoroethylene (PTFE) film and the Kapton film, the output performance generating by the mutual sliding friction between the FEP film and triboelectric power-generating units has a higher output.^[12] For the length of blade, there exists the maximum output performance when the length of blades is equal to that of a piece of electrode. Therefore, to achieve the maximum output performance, blades have dimensions of 75 mm (length) × 70 mm (width), 75 mm (length) × 60 mm (width), 75 mm (length) × 55 mm (width), which

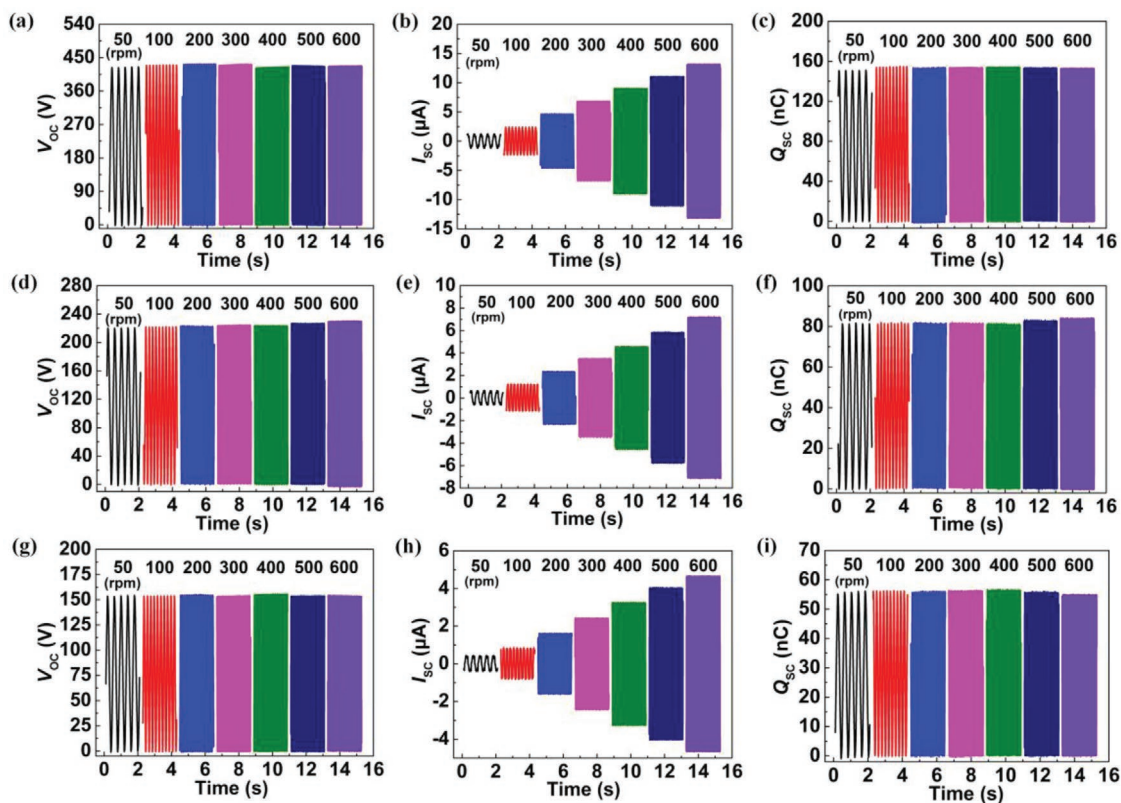


Figure 3. Electric output performance of one phase triboelectric power-generating unit of the DC-TENGs with a–c) 1P3G, d–f) 2P3G, and g–i) 3P3G at different rotation speeds.

correspond to the DC-TENG with three-group, four-group and five-group, respectively and the thickness of blades is 100 μm .

For the DC-TENG, the open-circuit voltage (V_{OC}), the short-circuit current (I_{SC}), and the transfer charge (Q_{SC}) could be expressed as^[13]

$$V_{OC} = \frac{\sigma S}{C} \quad (3)$$

$$I_{SC} = \frac{dQ}{dt} \quad (4)$$

$$Q_{SC} = \int I_{SC} dt \quad (5)$$

where σ is the density of transfer charge, S is the contact area between FEP films and electrodes, and C is the capacity.

To measure the output performance of the DC-TENGs, a rotation motor is employed to supply external incentive with different rotation speeds. **Figure 3** reveals V_{OC} , I_{SC} , and Q_{SC} of DC-TENGs with 1P3G, 2P3G, and 3P3G at various rotation speeds. According to the Equation (3), it can be seen that the values of the voltage are determined by the charge density and the contact area. Since the total area of the triboelectric power-generating unit of different DC-TENGs is the same, the charge density of the prototype is constant and thereby, the transfer charge Q_{SC} keeps almost constant with the increase of rotation

speed (see **Figure 3c,f,i**). What is more, because the contact area between the triboelectric power-generating unit and blades is constant, it is clear in **Figure 3a,d,g** that the V_{OC} remains almost unchanged with the increase of rotation speed. However, in accordance with Equation (4), with the increase of rotation speed, the current of the DC-TENG increases on the precondition of constant transfer charge (see **Figure 3b,e,h**). The working area of one phase triboelectric power-generating unit of the DC-TENG with 1P3G is twice as much as that of the DC-TENG with 2P3G and three times as much as that of the DC-TENG with 3P3G. And so the output performance between different DC-TENGs also has corresponding multiple relationships.

Furthermore, the influence of the number of groups of each phase triboelectric power-generating unit on the output performance of the TENG is investigated (see **Figure 4**). On the condition of keeping the number of phases unchanged, the number of groups of triboelectric power-generating units increases. It can be seen from **Figure 4b,e** that the output current of DC-TENG increases with the increase of the number of groups. However, as is shown in **Figure 4a,c,d,f**, the output voltage and charge remain almost unchanged since the contact area hardly changes. In addition, **Figure 4g–i** shows the output performance of one phase triboelectric power-generating unit in DC-TENGs. The working area of one phase triboelectric power-generating unit of the DC-TENG with 1P3G is twice as much as that of the DC-TENG with 2P3G and three times as much as

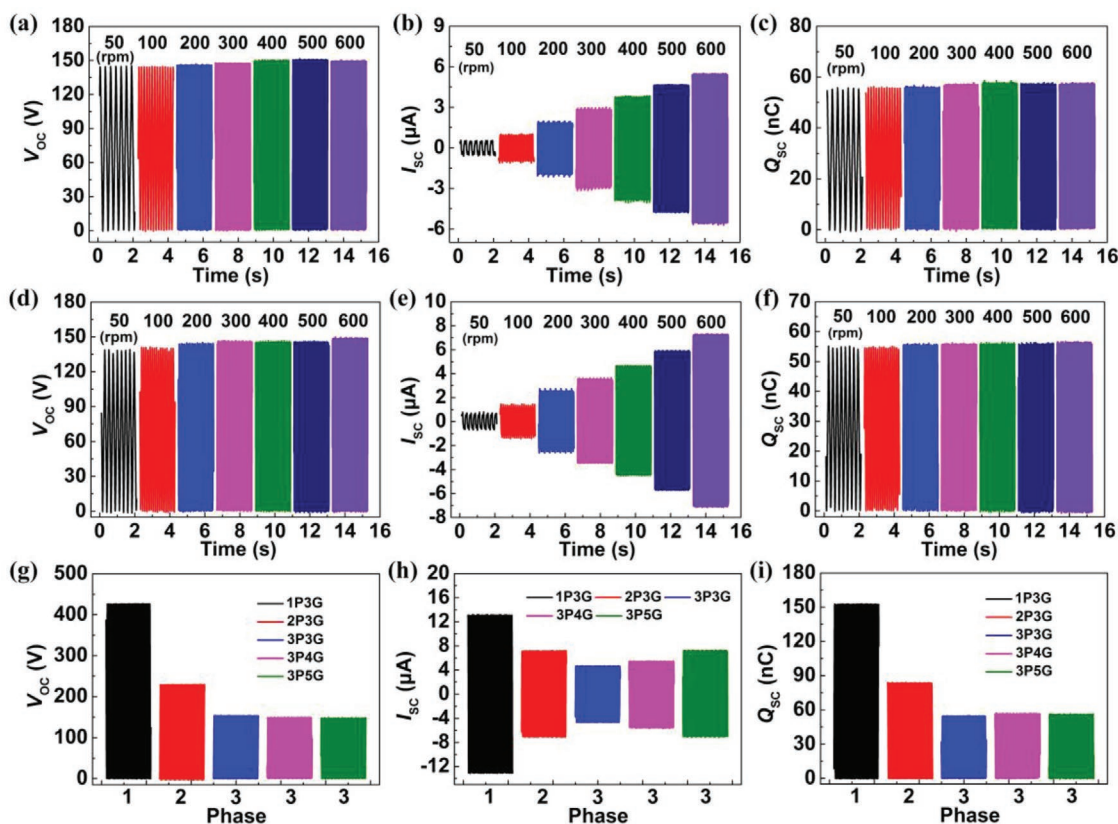


Figure 4. Electric output performance of the DC-TENGs. a–f) Electric output performance of one triboelectric power-generating unit of the DC-TENGs with a–c) 3P4G and d–f) 3P5G at different rotation speeds. g–i) Comparison diagram of electric output performance of the DC-TENGs with unanimous phases and different groups at 600 rpm.

that of the DC-TENG with 3P3G, 3P4G and 3P5G. And it could be found that the V_{oc} and Q_{sc} of one phase triboelectric power-generating unit in DC-TENG with 1P3G are twice as much as that with 2P3G and three times as much as that with 3P3G, 3P4G, and 3P5G. The I_{sc} of one phase triboelectric power-generating unit in DC-TENG with 1P3G, 2P3G and 3P3G have corresponding multiple relationships. However, the I_{sc} of one phase triboelectric power-generating unit in DC-TENG with 3P4G and 3P5G increase resulting from the increase of the number of groups. Therefore, the output current increases because the frequency of charge transfer increases and the current increases with the increase of groups.

To prove the feasibility of this scheme where the alternating current output rectified by a full-wave rectifier bridge is superimposed, Figure 5a–e shows the measured results of coupling current of the DC-TENGs at different rotation speeds. Because the programmable electrometer is a capacitive device, it measures the output performance of the TENGs by way of charging and discharging of the capacitor. However, due to the use of a full-wave rectifier bridge, the capacitor of programmable electrometer discharges insufficient in the process of capacitance charging and discharging. With the increase of rotation speed, the frequency of charge transfer of DC-TENG with 1P3G increases. Therefore, with an increase of rotation speed, the maximum and minimum values of the coupling current increase for the DC-TENG with 1P3G. Besides, for other

DC-TENGs, with an increase of rotation speed, the maximum and minimum values of the coupling current increase resulting from the superposition of each phase rectified current (see Figure 5b–e). For the DC-TENGs with 2P3G and 3P3G, as the number of phases increases from 2 to 3, the minimum values of the output current increase while the maximum current remains almost unchanged (see Figure 5b,c). For the DC-TENGs with 3P4G and 3P5G, as the number of groups increases from 4 to 5, the maximum and minimum values of the output current increase and the increase in the output performance from four-group to five-group are due to the increase of groups causing the increase of transfer frequency of electrons (see Figure 5f).

The DC-TENG is designed to increase root-mean-square value and decrease the crest factor, generating a constant DC output. To prove the feasibility of this structural design, Figure 6a–c shows the amplitude, the root-mean-square value, and the crest factor of the total output current. For details, the amplitude could be represented as

$$I_{AMP} = I_{max} - I_{min} \quad (6)$$

where I_{AMP} is the amplitude of the total output current, I_{max} is the maximum value of current, and I_{min} is the minimum value of the total output current.

The root-mean-square value is the most common mathematical method to define the effective voltage or current of a

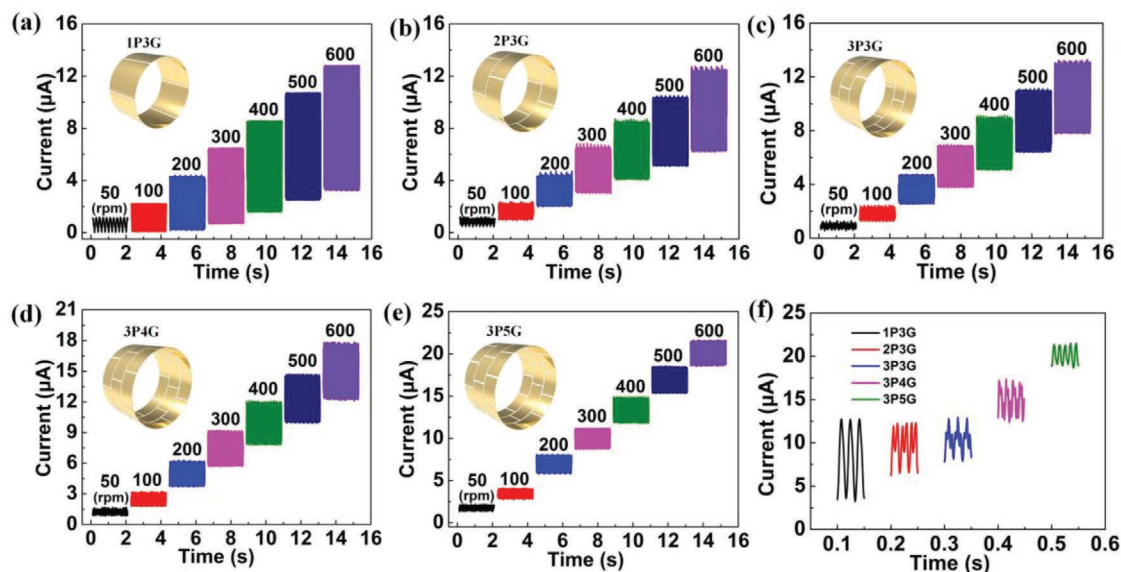


Figure 5. Schematic diagram of the coupling current of DC-TENGs. Diagrams of coupling current of the DC-TENGs with a) 1P3G, b) 2P3G, c) 3P3G, d) 3P4G, and e) 3P5G. f) Comparison diagram of coupling current of the DC-TENG with unanimous phases and different groups within 0.05 s at 600 rpm.

circuit. The root-mean-square value of output current could be represented as^[14]

$$I_{\text{rms}} = \sqrt{\frac{\int_0^T i^2 dt}{T}} \triangleq \sqrt{\frac{\sum_{j=1}^m I_j^2}{m}} \quad (7)$$

where I_j is the output current at different time points, and m is the number of time points.

The crest factor CF_x of current is defined as the ratio of its maximum value and the root-mean-square value, and it could be represented as^[15]

$$CF_x = \frac{I_{\text{max}}}{I_{\text{rms}}} \quad (8)$$

where I_{max} is the maximum value of current, and I_{rms} is the root-mean-square value of current.

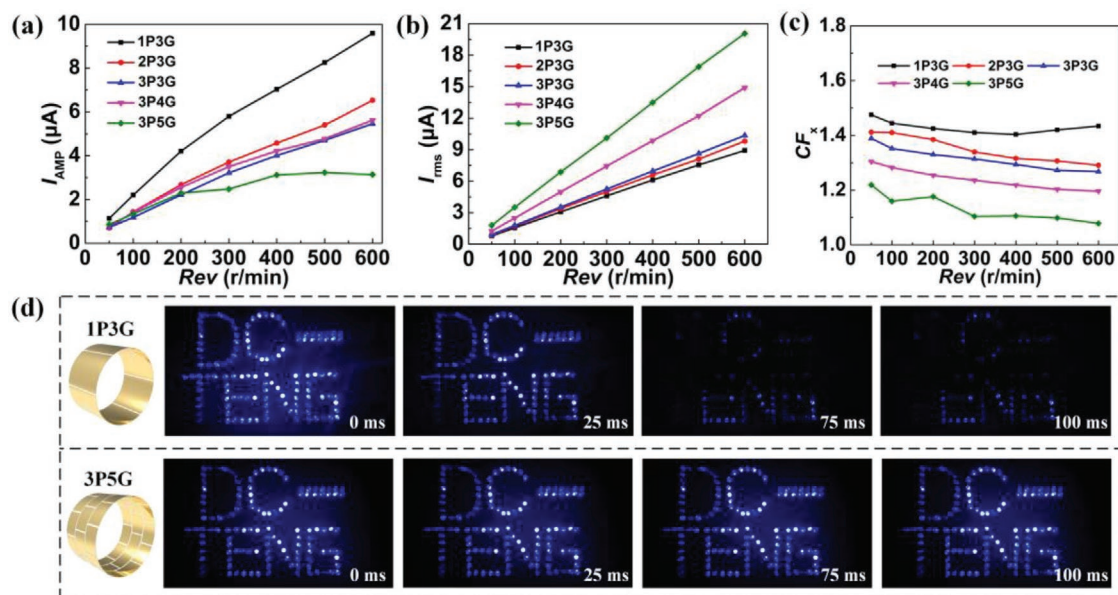


Figure 6. Schematic diagram of the output performance of the total output current among different DC-TENGs. a) Schematic diagram of current amplitude among different DC-TENGs at different rotation speeds. b) Schematic diagram of the root-mean-square value of the total output current among different DC-TENGs at different rotation speeds. c) Schematic diagram of the crest factor of total output current among different DC-TENGs at different rotation speeds. d) The performance comparison of video snapshots of DC-TENGs with 1P3G and 3P5G at 100 rpm.

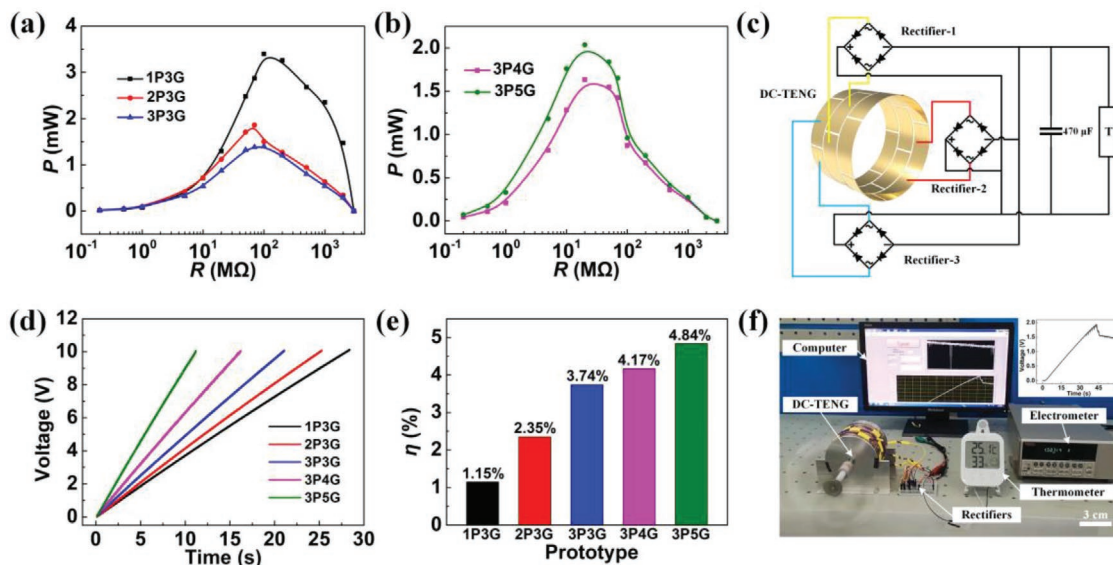


Figure 7. Demonstration and output performance of the DC-TENGs. a,b) Comparison of the total average output power of DC-TENGs with different phases and groups. c) The diagram of three-phase rectifier circuit for charging capacitors by the DC-TENG. d) Comparison of 22 μF capacitor charging behavior by various DC-TENGs at 600 rpm. e) The capacitance charging efficiency of the DC-TENGs. f) Demonstration of DC-TENG harvesting wind energy to power a thermometer (scale bar, 3 cm).

Figure 6 shows the comparison diagram of the output performance of the total output current among different DC-TENGs. As is depicted in Figure 6a, with the increase of the rotation speed, the amplitude of the total output current increases, and with the increase of the phases and groups, the amplitude of the total output current decreases in accordance with Equation (6). It can be seen from Figure 6b that with the increase of groups from 3 to 5 the average current has significant growth. Because the current waveform measured by a programmable electrometer is a series of sampling points, the RMS of current could be calculated by the second half of Equation (7). Figure 6c shows that with the increase of the rotation speed, the crest factor remains almost unchanged while with the increase of phases and groups, the crest factor has a significant decrease in accordance with the calculation of Equation (8). The DC-TENG could enhance the output performance utilizing increasing the phases and the groups to achieve the goal of producing an almost constant current. To demonstrate the superiority of the output performance of the DC-TENG with 3P5G, 121 light emitting diodes (LEDs) in series are illuminated by the DC-TENGs with 1P3G and 3P5G at 100 rpm at the same time, respectively. As is illustrated in Figure 6d, the flicker degree of “DC-TENG” LEDs remains almost unchanged illuminated by the DC-TENG with 3P5G within 100 ms compared with the DC-TENG with 1P3G. Thus, the DC-TENG with 3P5G can continuously provide energy to LEDs in the form of direct current. The phenomenon has proved the superiority of multiphase TENG that can generate an almost constant current of a low crest factor.

2.3. Demonstration

In order to study the output power characteristics of DC-TENGs, the current of the DC-TENGs with different phases

and groups is measured under different loads at a rotation speed of 600 rpm, respectively, and the average output power of the DC-TENG was calculated. What is more, all curves of average output power are put together and compared (see Figure 7a,b). As is depicted in Figure 7a, the maximum average output power (\bar{P}_{\max}) of the DC-TENG with 1P3G, 2P3G, and 3P3G is 3.40, 1.86, and 1.40 mW when the matching resistance is 100, 70, and 70 $\text{M}\Omega$, respectively. Due to the rectifier circuit in parallel, the matching resistance of DC-TENGs is reduced. The experimental results indicate that the total average output power of DC-TENGs has decreased with the increase of phases and the reason for this phenomenon can be explained by the following ones. The total average output power (\bar{P}) of DC-TENGs can be expressed as

$$\bar{P} = P I_R^2 R \quad (9)$$

where P is the number of phases ($P = 1, 2, 3$), I_R is the load current of one phase triboelectric power-generating unit of the DC-TENG with 1P3G, 2P3G, and 3P3G, respectively and R is the load impedance of external circuit.

As is illustrated in Table 2, the output performance of one phase triboelectric power-generating unit of the DC-TENG with 1P3G, 2P3G, and 3P3G decrease, which results in the decrease of total output performance.

As is depicted in Figure 7b, the maximum average output power (\bar{P}_{\max}) of the DC-TENG with 3P4G and 3P5G is 1.63 and 2.04 mW when the matching resistance is 20 and 20 $\text{M}\Omega$, respectively. The average output power of the DC-TENG has significantly increased, which is the reason why the frequency of charge transfer increases and the current increases with the increase of groups. Concrete information between the current and the average output power about DC-TENGs is depicted in Figure S5(Supporting Information).

Table 2. The angular relationship between each triboelectric power-generating unit.

	\bar{I}_R	R	\bar{P}
1P3G	I	R	I^2R
2P3G	$\frac{1}{2}I$	R	$\frac{1}{2}I^2R$
3P3G	$\frac{1}{3}I$	R	$\frac{1}{3}I^2R$

What is more, to investigate the capacitance charging efficiency of the DC-TENG with different phases and groups to harvest rotation energy, a commercial capacitor of 22 μF is adopted, and the rotational speed of the rotation motor is 600 rpm. As is depicted in Figure 7c, the method is adopted that the alternating current output rectified by a full-wave rectifier bridge is superimposed, and the direct-current output is gained.

It can be seen from Figure 7d that with the increase of phases and groups, the charging time of the DC-TENG has a significant shortening. The energy storage of capacitor (W) can be expressed as

$$W = 0.5CU_F^2 \quad (10)$$

where C is the capacity value of energy storage capacitor and U_F is the voltage that the capacitor can finally charge.

Thus, the power of charging the capacitor by the DC-TENG (P_F) can be calculated by the following Equation (11)

$$P_F = \frac{W}{t} \quad (11)$$

where t is the required time that charges the capacitor to a certain voltage value.

Therefore, the capacitance charging efficiency (η) of the prototype is calculated by Equation (12)

$$\eta = \frac{P_F}{\bar{P}_{\max}} \quad (12)$$

where \bar{P}_{\max} is the maximum average output power of the DC-TENGs.

As is shown in Figure 7e, the experimental data of capacitance charging efficiency indicate that the charging performance of DC-TENG with 3P3G is almost three times than that of DC-TENG with 1P3G. For the DC-TENG with 3P5G, it has more groups of electrodes than that with 3P3G, the frequency of electron transfer increases, and a greater current is generated, which results in the increase of total output performance.

In addition, the capacity for energy storage and powering a commercial thermometer is demonstrated in Figure 7f. The shaft of the prototype is connected with the vane by a coupling. The DC-TENG is driven by a blowing machine, and the wind speed is about 13.9 m s^{-1} . A capacity of 470 μF is employed to store the electrode energy and then powering a thermometer. The detailed experiment displayed in Video S2 (Supporting Information).

What is more, to prove its practical feasibility, the experiments have been done for validating charging performance at lower wind speed (see Video S4, Supporting Information). And the DC-TENG can illumine 249 light emitting diodes (LEDs) in series as shown in Video S3 (Supporting Information). The results indicate that the DC-TENG can be employed to harvest wind energy around the ambient environment.

3. Conclusions

A high-performance cylindrical direct-current triboelectric nanogenerator (DC-TENG) is reported in the paper, which utilizes freestanding triboelectric-layer mode and phase coupling. The proposed DC-TENG consists of a rotator and a cylindrical stator. Each phase triboelectric power-generating unit regularly shifted on the cylindrical stator produces a current output of almost identical frequency, equal amplitude and initial phase delayed in turn. And then, the output current rectified by the full-wave rectifier bridge is superimposed, and the DC-TENG could produce an almost constant current with a low crest factor of 1.08. The charging efficiency of the DC-TENG with three-phase and five-group is three times higher than that of the DC-TENG with single-phase three-group resulting from the almost constant current output. The experimental results show that with the increase of phases, a constant direct-current output with a low crest factor is provided, and with the increase of groups, the total output performance has obtained a remarkable enhancement. In summary, the research is of great significance to the practical applications of triboelectric nanogenerators in powering sensors.

4. Experimental Section

Fabrication of the DC-TENG: The DC-TENG was composed of a stator and a rotator. The stator was composed of an acrylic barrel, two end-caps, two bearings (Model: SC6700zz, NSK, Japan), two supports, and triboelectric power-generating units. The external diameter and inner diameter of the acrylic barrel were 115 and 109 mm, respectively. Two end-caps and two supports whose main raw materials were stainless steel were machined by a milling machine. And two bearings were obtained commercially. The dimension of triboelectric power-generating units whose materials were copper was 66 mm (height) \times 109 mm (diameter). For details, two end-caps fixed on two bearings were integrated with the acrylic barrel on its top and bottom sides (to stabilize the shaft of the rotator). And the acrylic barrel was placed in two supports, and the triboelectric power-generating unit adhered to the inner wall of the acrylic barrel. The rotator consisted of a shaft, a reel, and several blades. The shaft, whose main raw material was stainless steel, was machined by a lathe, and its size was 160 mm (length) \times 10 mm (diameter). For the reel with a dimension of 75 mm (length) \times 99 mm (diameter), its main raw material was acrylonitrile butadiene styrene (ABS), which was processed by a milling machine. The flexible blades evenly distributing around the reel were fluorinated ethylene propylene (FEP) films with a thickness of 100 μm and a width of 75 mm and were connected with the reel using gelatin sponges with a dimension of 75 mm (length) \times 10 mm (width). Additional details are available in Supporting Information.

Measurement of the DC-TENG: The external incentives were provided by a rotation motor (Model: J-5718HBS401, Yisheng, China), which was connected with the DC-TENG by a rigid coupling and an industrial

speed blower (Model: 070020B, MNT, China). The output wires from the DC-TENG was connected to a programmable electrometer (Model: 6514, Keithley, USA), which connected to a data acquisition system (Model: PCI-6259, National Instruments, USA) and a computer. A programmed LabVIEW software was conducted to collect the electric output signal and store it.

Supporting Information

Supporting Information is available from the Wiley Online Library or from the author.

Acknowledgements

J.W., Y.L., and Z.X. contributed equally to this work. The authors are grateful for the support received from the National Key R & D Project from Minister of Science and Technology (2016YFA0202704), the Beijing Municipal Science and Technology Commission (Z171100002017017), and the National Natural Science Foundation of China (grant numbers 51775130).

Conflict of Interest

The authors declare no conflict of interest.

Keywords

direct current, energy harvesting, low crest factor, phase coupling, triboelectric nanogenerators

Received: December 24, 2019

Revised: January 23, 2020

Published online:

- [1] a) Z. L. Wang, *ACS Nano* **2013**, *7*, 9533; b) R. Hinchet, H. J. Yoon, H. Ryu, M. K. Kim, E. K. Choi, D. S. Kim, S. W. Kim, *Science* **2019**, *365*, 491; c) M. Xu, P. Wang, Y. Wang, S. L. Zhang, Z. L. Wang, *Adv. Energy Mater.* **2018**, *8*, 1702432.
- [2] a) C. Bo, Y. Yang, Z. L. Wang, *Adv. Energy Mater.* **2018**, *8*, 1702649; b) G. Zhu, P. Bai, J. Chen, Q. Jing, Z. L. Wang, *Nano Energy* **2015**, *14*, 126; c) Z. L. Wang, *Faraday Discuss.* **2015**, *176*, 447.
- [3] a) F. R. Fan, Z. Q. Tian, Z. L. Wang, *Nano Energy* **2012**, *1*, 328; b) Z. L. Wang, A. C. Wang, *Mater. Today* **2019**, *30*, 34.
- [4] a) S. Niu, S. Wang, L. Lin, Y. Liu, Y. S. Zhou, Y. Hu, Z. L. Wang, *Energy Environ. Sci.* **2013**, *6*, 3576; b) S. Niu, Y. Liu, S. Wang, L. Lin, Y. S. Zhou, Y. Hu, Z. L. Wang, *Adv. Mater.* **2013**, *25*, 6184; c) S. Niu, Y. Liu, S. Wang, L. Lin, Y. S. Zhou, Y. Hu, Z. L. Wang, *Adv. Funct. Mater.* **2014**, *24*, 3332.
- [5] a) M.-L. Seol, J.-W. Han, D.-I. Moon, K. J. Yoon, C. S. Hwang, M. Meyyappan, *Nano Energy* **2018**, *44*, 82; b) T. Guo, G. Liu, Y. Pang, B. Wu, F. Xi, J. Zhao, T. Bu, X. Fu, X. Li, C. Zhang, Z. L. Wang, *Extreme Mech. Lett.* **2018**, *18*, 1; c) J. Qian, X. Wu, D.-S. Kim, D.-W. Lee, *Sens. Actuators, A* **2017**, *263*, 600; d) C. Yan, Y. Gao, S. Zhao, S. Zhang, Y. Zhou, W. Deng, Z. Li, G. Jiang, L. Jin, G. Tian, T. Yang, X. Chu, D. Xiong, Z. Wang, Y. Li, W. Yang, J. Chen, *Nano Energy* **2020**, *67*, 104235.
- [6] a) Z. L. Wang, *Mater. Today* **2017**, *20*, 74; b) L. Jin, B. Zhang, L. Zhang, W. Yang, *Nano Energy* **2019**, *66*, 104086.
- [7] a) J. Wang, Z. Wu, L. Pan, R. Gao, B. Zhang, L. Yang, H. Guo, R. Liao, Z. L. Wang, *ACS Nano* **2019**, *13*, 2587; b) C. Zhang, T. Zhou, W. Tang, C. Han, L. Zhang, Z. L. Wang, *Adv. Energy Mater.* **2014**, *4*, 1301798.
- [8] a) J. Luo, L. Xu, W. Tang, T. Jiang, F. R. Fan, Y. Pang, L. Chen, Y. Zhang, Z. L. Wang, *Adv. Energy Mater.* **2018**, *8*, 1800889; b) Y. Yang, H. Zhang, Z. L. Wang, *Adv. Funct. Mater.* **2014**, *24*, 3745; c) D. Liu, X. Yin, H. Guo, L. Zhou, Z. L. Wang, *Sci. Adv.* **2019**, *5*, eaav6437.
- [9] a) S. Lin, Y. Lu, S. Feng, Z. Hao, Y. Yan, *Adv. Mater.* **2019**, *31*, 1804398; b) H. Shao, J. Fang, H. Wang, H. Zhou, T. Lin, *J. Mater. Chem. A* **2017**, *5*, 8267; c) J. Liu, A. Goswami, K. Jiang, F. Khan, S. Kim, R. McGee, Z. Li, Z. Hu, J. Lee, T. Thundat, *Nat. Nanotechnol.* **2018**, *13*, 112; d) H. Shao, J. Fang, H. Wang, H. Zhou, H. Niu, F. Chen, G. Yan, S. Fu, Y. Cao, T. Lin, *Adv. Electron. Mater.* **2018**, *5*, 1800675; e) H. Shao, J. Fang, H. Wang, L. Dai, T. Lin, *Adv. Mater.* **2016**, *28*, 1461.
- [10] a) T. Kim, D. Y. Kim, J. Yun, B. Kim, S. H. Lee, D. Kim, S. Lee, *Nano Energy* **2018**, *52*, 95; b) H. Ryu, J. H. Lee, U. Khan, S. S. Kwak, R. Hinchet, S.-W. Kim, *Energy Environ. Sci.* **2018**, *11*, 2057.
- [11] a) A. A. Teklu, R. M. Sullivan, *J. Electrostat.* **2017**, *86*, 34; b) C. He, C. B. Han, G. Q. Gu, T. Jiang, B. D. Chen, Z. L. Gao, Z. L. Wang, *Adv. Energy Mater.* **2017**, *7*, 1700644.
- [12] P. Wang, L. Pan, J. Wang, M. Xu, G. Dai, H. Zou, K. Dong, Z. L. Wang, *ACS Nano* **2018**, *12*, 9433.
- [13] a) H. Y. Guo, Z. Wen, Y. L. Zi, M. H. Yeh, J. Wang, L. P. Zhu, C. G. Hu, Z. L. Wang, *Adv. Energy Mater.* **2016**, *6*, 1501593; b) S. Wang, Y. Xie, S. Niu, L. Lin, Z. L. Wang, *Adv. Mater.* **2014**, *26*, 2818.
- [14] T. Chai, R. R. Draxler, *Geosci. Model Dev.* **2014**, *7*, 1247.
- [15] P. Guillaume, J. Schoukens, R. Pintelon, I. Kollar, *IEEE Trans. Instrum. Meas.* **2015**, *40*, 982.